RSC Advances

PAPER

View Article Online
View Journal | View Issue

Cite this: *RSC Adv.*, 2024, **14**, 7329

Effects of magnesium hydroxide morphology on Pb(ii) removal from aqueous solutions†

Donghai Zhu, ‡* Jiachen Zhu,‡ Ping Li and Shengjie Lan*

In this study, magnesium hydroxide (MH) particles with distinct morphologies were obtained through direct precipitation and subsequent hydrothermal treatment with various magnesium salts. The synthesized products were systematically characterized and utilized for the removal of Pb(II) ions from aqueous solutions. The adsorption process of Pb(II) by two different MH structures, namely flower globular magnesium hydroxide (FGMH) and hexagonal plate magnesium hydroxide (HPMH), adhered to the Langmuir isotherm and pseudo-second-order model. FGMH exhibited higher Pb(II) removal capacity (2612 mg g^{-1}) than HPMH (1431 mg g^{-1}), attributable to the unique three-dimensional layered structures of FGMH that provide a larger surface area and abundant active sites. Additionally, metallic Pb was obtained by recycling the adsorbed Pb(II) through acid dissolution-electrolysis. Furthermore, Pb(II) removal mechanisms were investigated by analyzing adsorption kinetics and isotherms, and the adsorbed products were characterized. Based on the findings, the removal process occurs in two key stages. First, Pb(II) ions bind with OH^- ions on the surface upon diffusing to the MH surface, resulting in $Pb(OH)_2$ deposits *in situ*. Concurrently, Mg(II) ions diffuse into the solution, substituting Pb(II) ions in the MH lattice. Second, the resultant $Pb(OH)_2$, which is unstable, reacts with CO_2 dissolved in water to yield $Pb_3(CO_3)_2(OH)_2$. Therefore, owing to its outstanding Pb(II) adsorption performance and simple preparation method, FGMH is a promising solution for Pb(II) pollution.

Received 23rd November 2023
Accepted 28th February 2024

DOI: 10.1039/d3ra08040d

rsc.li/rsc-advances

1. Introduction

Heavy metals are naturally present in the environment at certain concentrations. However, rapid industrialization, encompassing processes such as smelting, chemical manufacturing, electroplating, plastics production, and battery manufacturing, has led to an increased emission of heavy metal ions into the environment, particularly water sources.[1,2] These heavy metal ions can infiltrate the food chain through water and soil, even in trace amounts, eventually accumulating in living organisms where they become challenging to degrade. When heavy metal ions reach a certain concentration, they can interfere with the functional groups essential for biomolecule activity, displace necessary metal ions within biomolecules, alter the conformation or higher-level structure of biomolecules, and consequently lead to biological dysfunction and various diseases.[3,4] For example, as a highly toxic heavy metal ion, Pb(II) can not only cause neurotoxicity in humans and animals, but also impede photosynthesis in plants and suppress the growth.[5,6] Therefore, the treatment of heavy metal-contaminated wastewater has emerged as an urgent environmental concern.

Several methods are employed for treating heavy metal-contaminated water, including membrane separation,[7] ion exchange,[8] electrochemical treatment,[9] chemical precipitation,[10] and adsorption.[11] Among these techniques, adsorption stands out owing to its relative simplicity, low energy consumption, operational cost, minimal raw material expenses, and absence of secondary pollution issues.[12] Studies have reported the use of various materials such as zeolite,[13] clay,[14] activated alumina,[15] activated carbon,[16] graphene,[17] carbon nanotubes,[18] and chitosan[19] for adsorbing heavy metal ions from wastewater. However, these materials either prove ineffective for low-concentration heavy metal wastewater or are prohibitively expensive for large-scale industrial applications. Therefore, research efforts must be dedicated to developing materials with high removal capacity, low cost, and high efficiency for removing heavy metal ions.

In recent years, metal hydroxides and metal oxides have attracted considerable attention as adsorbents owing to their affordability, excellent adsorption properties, and environmental friendliness.[20,21] Notably, micro/nanosized magnesium hydroxide (MH) has emerged as a promising candidate for heavy metal removal. For example, Jiang *et al.* reported that flower-shaped globular MH could remove 92.6% of Ni(II)

State Key Laboratory of Plateau Ecology and Agriculture, School of Chemical Engineering, Qinghai University, Xining 810016, PR China. E-mail: zhudonghai-2001@163.com; lanshengjie@126.com

† Electronic supplementary information (ESI) available. See DOI: https://doi.org/10.1039/d3ra08040d

‡ Donghai Zhu and Jiachen Zhu contributed equally to this work.

ions from wastewater through chemical adsorption.[22] Zhu *et al.* demonstrated that coral-like hierarchical porous MH exhibited desirable adsorption performance and removed Pb(II) and Cd(II) ions from wastewater through solid–liquid interfacial reactions.[23] Additionally, Amrulloh *et al.* reported that nano-flake MH exhibits remarkably high adsorption capacity for Cd(II) and Pb(II) ions and good reusability over more than six cycles.[24] Typically, the adsorption performance of MH is notably influenced by its microstructure, with different morphologies of MH exhibiting distinct microstructures. Ideally, the morphology of MH should provide a large specific surface area, an abundance of active sites, and a suitable size, satisfying mechanical strength requirements and facilitating recovery. However, obtaining MH with these desired characteristics often necessitates the use of structure-directing molecules or crystal modifiers, leading to increased production costs.

In this study, MH particles with different morphologies were prepared by varying the magnesium sources and hydrothermal conditions, all without using structure-directing molecules or crystal modifiers. The products were characterized and then employed to remove Pb(II) ions from aqueous solutions. The adsorption capabilities of two distinct morphologies of MH for Pb(II) ions were evaluated and compared. Furthermore, to promote resource utilization, the recycling of Pb(II) ions adsorbed by MH through acid dissolution-electrolysis into metallic Pb was explored. Moreover, the mechanism of Pb(II) ion adsorption on MH was determined by analyzing adsorption kinetics and adsorption isotherms and characterizing adsorbed products.

2. Experimental

2.1 Materials

$MgSO_4 \cdot 7H_2O$, $MgCl_2 \cdot 6H_2O$, HNO_3, NaOH, and $Pb(NO_3)_2$ were of analytical research grade and supplied by Sinopharm Chemical Reagent Co., Ltd (Shanghai, China). Ammonia solution ($NH_3 \cdot H_2O$: 25%) was purchased from Shuangshuang Chemical Co., Ltd (Yantai, China).

2.2 Synthesis of MH

Flower globular magnesium hydroxide (FGMH) was synthesized through direct precipitation. First, 24.65 g of $MgSO_4 \cdot 7H_2O$ was dissolved in 50 mL of deionized water and heated at 60 °C. Subsequently, 150 mL of ammonia was added dropwise using a pipette to the solution while stirring at a speed of 850 rpm. Thereafter, the reaction solution was allowed to age for 2 h. The suspension was centrifuged and washed. The resulting precipitate was collected and freeze-dried to obtain FGMH.

Hexagonal plate magnesium hydroxide (HPMH) was synthesized through a hydrothermal process. In a standard procedure, 40 mL of a 3.45 mol L^{-1} $MgCl_2 \cdot 6H_2O$ was heated at 60 °C. Subsequently, 30 mL of ammonia solution was added dropwise using a pipette while stirring at a speed of 850 rpm. Thereafter, the slurry was transferred to an autoclave and reacted at 170 °C for 6 h. The obtained precipitate was filtered, washed and dried at 105 °C for 12 h to yield HPMH.

2.3 Adsorption experiments

Pb(II) solutions with different concentrations were prepared using $Pb(NO_3)_2$ as the source of heavy metal ions. The pH value of each Pb(II) solution was varied using NaOH (0.1 mol L^{-1}) and HNO_3 (0.1 mol L^{-1}).

Kinetic experiments were performed with 10 mg of MH with various morphologies added separately into 160 mL of 100 mg L^{-1} Pb(II) solution at pH 5 and 25 °C and agitated in an orbital shaker. After specific time intervals, samples were withdrawn and filtered through a 0.45 μm polyether sulfone membrane. The concentration of Pb(II) and Mg(II) ions in the filtrates was determined using a ZEEnit 700 P atomic absorption spectrometer (Analytik Jena, Germany).

Adsorption isotherm experiments were performed by following the aforementioned procedure at pH 5 and 25 °C for 4 h, with the exception that metal ion solutions with different concentrations ranging from 100 to 350 mg L^{-1} were used. All the experiments were conducted in duplicate. The Pb(II) ion removal efficiency (E%) and the adsorption capacity (q_t) of MH were calculated using formulae shown in the ESI.†

2.4 Characterization

The X-ray diffraction (XRD) patterns of the specimens were performed at a scan speed of 5° min^{-1} using a D5000 X-ray diffractometer (Karlsruhe, Germany) with Cu Kα radiation (λ = 0.1542 nm). The morphology and dimensions of the specimens were characterized using a JSM 6700 field emission scanning electron microscope (FESEM) equipped with an energy-dispersive X-ray spectrometer (EDS, JEOL, Japan). The porosity structure parameters of the specimens were evaluated using an ASAP 2020 Brunauer–Emmett–Teller (BET) surface area analyzer (Micromeritics Instrument Corp., USA).

3. Results and discussion

3.1 Specimen characterization

The morphologies of MH in the solutions prepared using different magnesium salts were observed through SEM. As illustrated in Fig. 1a, flower globular magnesium hydroxide (FGMH) with particle diameters of 2–5 μm was synthesized through chemical precipitation using $MgSO_4 \cdot 7H_2O$. An enlarged image (Fig. 1b) further indicates that each flower-shaped structure was composed of interconnected ultra-thin nanoplates, forming a spherical self-supporting structure. Fig. 1c illustrates hexagonal plate magnesium hydroxide (HPMH), which was synthesized through the hydrothermal method using $MgCl_2 \cdot 6H_2O$. An enlarged image (Fig. 1d) highlights that the hexagonal plates measured 0.5–3 μm in diameter, with a thickness substantially greater than that of the nanoplates in FGMH.

The crystalline phase of the products prepared using different magnesium sources was determined through XRD. As displayed in Fig. 2, the diffraction peaks of both FGMH and HPMH were well indexed as hexagonal $Mg(OH)_2$ (JCPDS, no. 44-1482).[24] Specifically, 2θ values at 18.60°, 32.88°, 38.04°, 50.88°, 58.71°, 62.16°, 68.30°, and 72.13° corresponded to the (001),

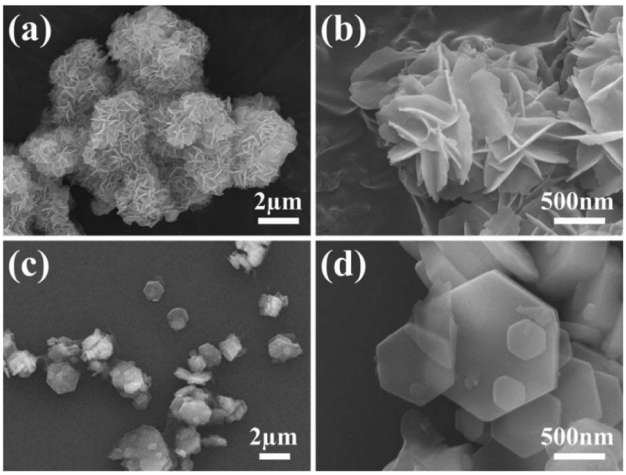

Fig. 1 SEM images of (a, b) FGMH and (c, d) HPMH.

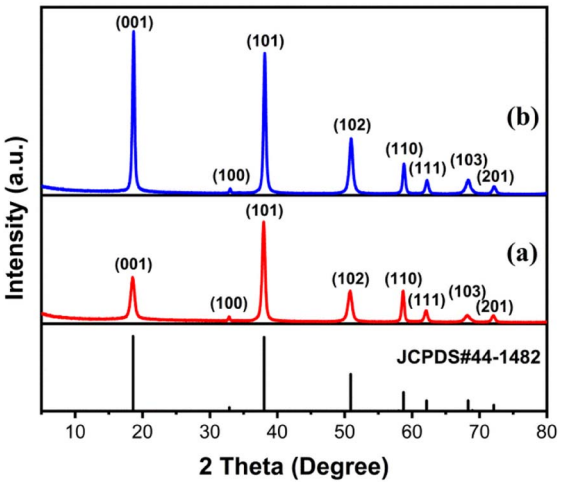

Fig. 2 XRD patterns of (a) FGMH and (b) HPMH.

(100), (101), (102), (110), (111), (103), and (201) planes, respectively. Interestingly, the (101) crystal plane diffraction peak of FGMH was the most prominent, while the (001) crystal plane diffraction peak of HPMH was the strongest. This phenomenon can be attributed to the alteration in crystal plane growth rates induced by hydrothermal treatment, leading to the formation of MH with varying morphologies.

The pore structure characteristics of MH with distinct morphologies were inferred from nitrogen adsorption–desorption isotherms. As indicated by Fig. 3a, both FGMH and HPMH exhibited characteristics resembling type-IV isotherms and type-H3 hysteresis loops.[21] Calculated using the BET and BJH model, the surface area and pore volume of FGMH were 60.46 $m^2 g^{-1}$ and 0.60 $m^3 g^{-1}$, respectively, significantly exceeding those of HPMH (with a surface area of 8.70 $m^2 g^{-1}$ and a pore volume of 0.08 $m^3 g^{-1}$). The pore size distribution of both FGMH and HPMH primarily ranged from 10 to 40 nm, indicative of mesoporous structural characteristics (Fig. 3b). The large surface area of FGMH can be attributed to the flower-globular structure assembled by MH nanosheets that prevents nanosheet agglomeration, resulting in a stable support structure with more pores.

3.2 Adsorption studies

3.2.1 Effects of pH values. The removal of Pb(II) using MH is influenced by solution pH values. In this study, the variations in solution pH values from 2 to 6 were analyzed, and the results are presented in Fig. 4. Within the pH range of 2 to 6, the removal efficiency of Pb(II) by FGMH increases with increasing pH values. The removal efficiency of Pb(II) remains low when solution pH values are between 2 and 3. This phenomenon can be attributed to the fact that FGMH is mostly dissolved due to neutralization. Therefore, FGMH is not suitable for adsorption of Pb(II) under strong acid conditions. When the solution pH value reaches 4, the removal efficiency of Pb(II) improves substantially. When the solution pH value increases to 5, the removal efficiency of Pb(II) is approximately 90%, with nearly complete removal at a solution pH of 6. To minimize the influence of complexation reactions between Pb(II) and OH^- when the solution pH exceeds 6, subsequent experiments were conducted with a pH value of 5.

3.2.2 Adsorption kinetics. The adsorption kinetics of MH with two different morphologies were compared, and the results are presented in Fig. 5. The adsorption rate of Pb(II) on FGMH

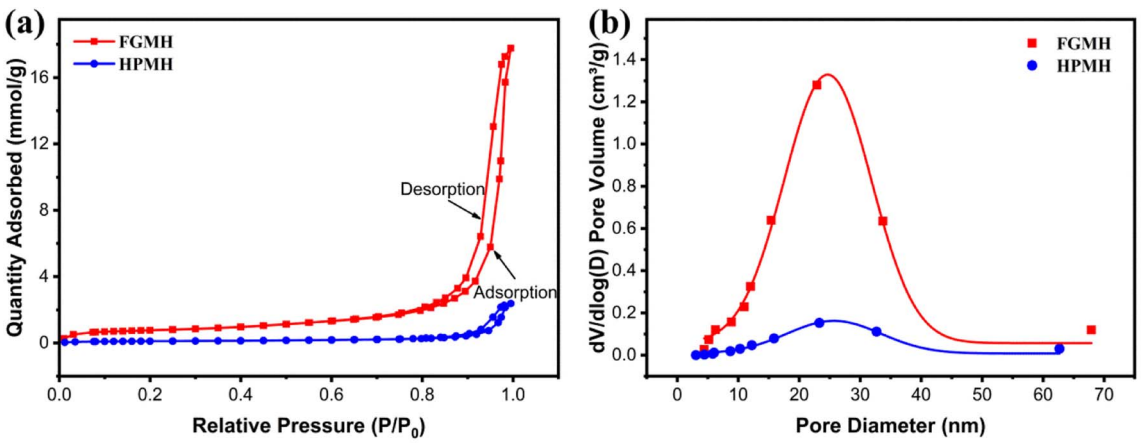

Fig. 3 (a) Nitrogen adsorption–desorption isotherms and (b) pore size distributions for FGMH and HPMH.

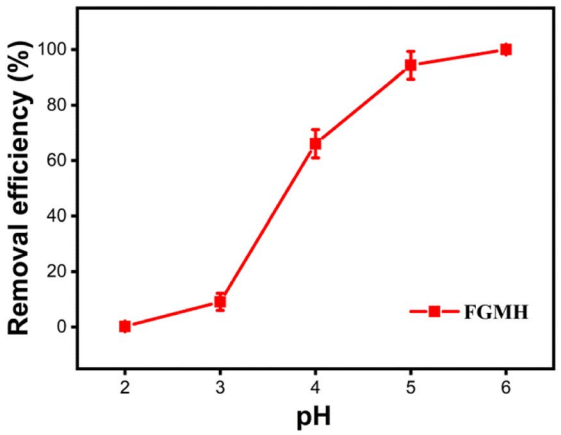

Fig. 4 Influence of solution pH values on the removal of Pb(II) with FGMH ($C_{Pb(II)}$: 100 mg L^{-1}, amount of adsorbent *m*: 10 mg, solution volume *V*: 160 mL, time *t*: 480 min).

was high in the first 60 min and reached equilibrium in 240 min. By contrast, the adsorption rate of Pb(II) on HPMH was lower, increasing the duration to reach equilibrium. Furthermore, the adsorption capacity of Pb(II) on FGMH was significantly higher than that on HPMH during the same timeframe.

To further investigate adsorption kinetics, the experimental data were fitted with pseudo-first-order and pseudo-second-order kinetic models, as expressed in the ESI.† The fitting results are displayed in Fig. 6. The fitted kinetic data with correlation coefficient (R^2) values are summarized in Table 1. The pseudo-second-order kinetic model more accurately predicts the adsorption of Pb(II) by FGMH, with a higher fitting R^2 value of 0.9942 compared to the pseudo-first-order kinetic model (0.9485). The experimentally measured adsorption capacity (1359 mg g^{-1}) closely aligns with the value calculated by the pseudo-second-order kinetic model (1435 mg g^{-1}), indicating chemical adsorption during the process. For HPMH, both the pseudo-second-order kinetic model and the pseudo-first-order kinetic model exhibit R^2 values greater than 0.9. Additionally, the maximum adsorption capacity of Pb(II) for HPMH calculated by the pseudo-second-order kinetic model (869 mg g^{-1}) closely matches the experimental adsorption capacity of 819 mg g^{-1}. These results suggest that the adsorption rate of Pb(II) by HPMH is also determined by the chemical adsorption.

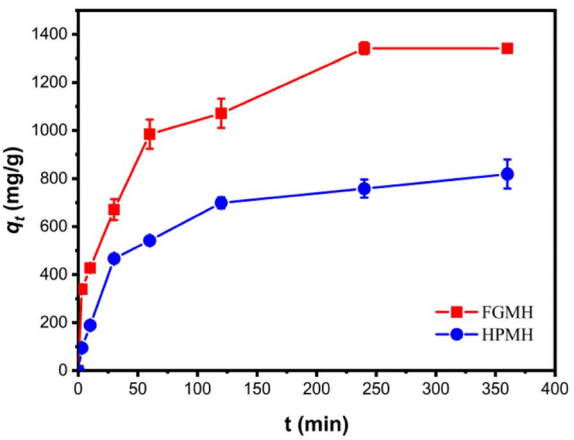

Fig. 5 Contrasting effects of contact time on Pb(II) adsorption with FGMH and HPMH (pH: 5, $C_{Pb\ (II)}$: 100 mg L^{-1}, amount of adsorbent *m*: 10 mg, solution volume *V*: 160 mL).

3.2.3 Adsorption isotherms. To gain insights into the adsorption process, the adsorption isotherms of Pb(II) on both FGMH and HPMH were evaluated using the Langmuir model and the Freundlich model, as expressed in the ESI.† The fitting results are presented in Fig. 7 and Table 2. Based on the obtained correlation coefficient (R^2), the Langmuir model more accurately characterizes the adsorption isotherm of Pb(II) on FGMH compared to the Freundlich model. In the case of Pb(II) adsorption onto HPMH, the Langmuir model aligns more closely with the experimental data. These findings indicate that the interaction between Pb(II) and MH of both morphologies primarily involves single molecule adsorption. The maximum adsorption capacities (q_m) for Pb(II), calculated using the Langmuir isotherm model, were determined to be 2612 mg g^{-1} for FGMH and 1431 mg g^{-1} for HPMH. These values closely match the experimental data (2544 mg g^{-1} for FGMH and 1240 mg g^{-1} for HPMH). Furthermore, considering the value of $1/n$, the adsorption effectiveness of Pb(II) by FGMH surpasses that of HPMH. This is attributable to the numerous nanosheets that constitute FGMH, resulting in a larger specific surface area and more active adsorption sites. In addition, the Pb(II) adsorption capacity of FGMH was compared with that of several typical adsorbents, as detailed in Table 3. The results show that the Pb(II) removal capability of the FGMH prepared in this study is much better than that of most other types of adsorbents and flower-like MH prepared without using structure-directing molecules. Compared with the coral-like hierarchical porous MH prepared with the addition of citric acid (structure-directing molecule), the FGMH prepared in this study still has excellent removal ability for Pb(II) at a lower pH, and holds promise as an effective and low-cost adsorbent for lead removal.

3.2.4 Effect of coexisting cations. Industrial wastewater often contains multiple coexisting cations (like Na^+, K^+, Co^{2+}, Ni^{2+}, Cu^{2+} and Zn^{2+}), resulting in competitive adsorption of

Table 1 Parameters of the kinetic models for Pb(II) adsorption on different MH particles

	Pseudo-first-order			Pseudo-second-order		
Sample	q_e (mg g^{-1})	K_1 (min^{-1})	R^2	q_e (mg g^{-1})	K_2 (g mg^{-1} min^{-1})	R^2
FGMH	1235	0.01645	0.9485	1435	2.75×10^{-5}	0.9942
HPMH	745	0.0082	0.9940	869	3.67×10^{-5}	0.9982

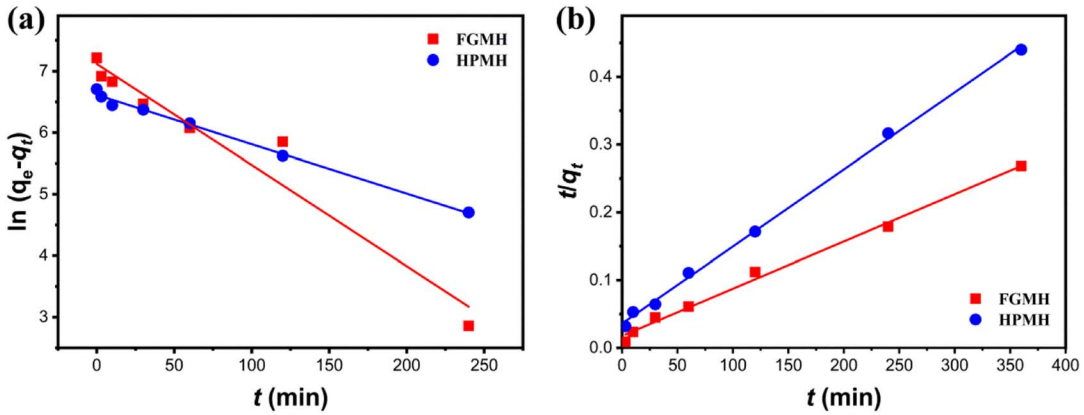

Fig. 6 (a) Pseudo-first-order and (b) pseudo-second-order kinetic models for the Pb(II) adsorption onto FGMH and HPMH (pH: 5, $C_{Pb(II)}$: 100 mg L^{-1}, amount of adsorbent m: 10 mg, solution volume V: 160 mL).

binding sites on the surface of adsorbents. In this work, the effect of above single coexisting cations with initial concentration of 100 mg L^{-1} on the adsorption capacity of FGMH and HPMH for Pb(II) was investigated. As shown in Fig. 8, the adsorption capacity of FGMH decreased from 1359 mg g^{-1} in aqueous solution to 1318, 1316 1201, 1192, 1105 and 1250 mg g^{-1} in the presence of single Na^+, K^+, Co^{2+}, Ni^{2+}, Cu^{2+} and Zn^{2+}, respectively. Besides Na^+ and K^+ ions, other coexisting ions (Co^{2+}, Ni^{2+}, Cu^{2+} and Zn^{2+}) have a certain inhibitory effect on the remove of Pb(II). The effect of these coexisting ions on the adsorption capacity of HPMH is similar. This can be attributed to the fact that the Co^{2+}, Ni^{2+}, Cu^{2+} and Zn^{2+} can also combine with the hydroxyl on the surface, which hinders the ion exchange between Pb(II) and Mg(II). Fortunately, both FGMH and HPMH could still have high adsorption capacity in the presence of these coexisting ions.

3.3 Electrolytic recycling

To prevent secondary pollution from adsorption products and to recycle lead resources,[33] metallic lead was recovered from solid products after treating Pb(II) solution through acid dissolution-electrolysis (Experimental section shown in ESI†).

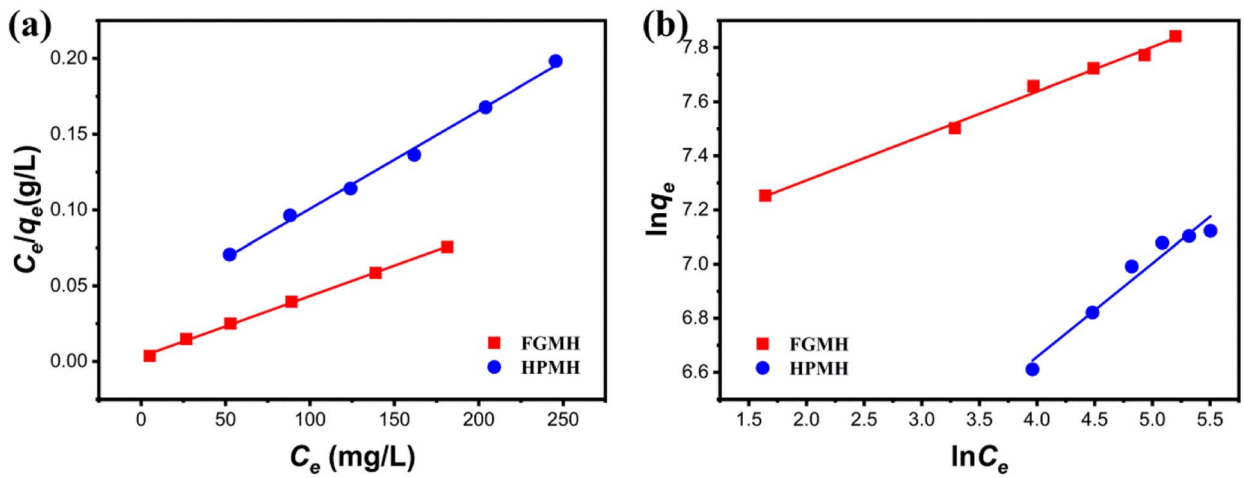

Fig. 7 (a) Langmuir and (b) Freundlich isotherm models for Pb(II) adsorption onto FGMH and HPMH (pH: 5, amount of adsorbent m: 10 mg, solution volume V: 160 mL, time t: 240 min).

Table 2 Parameters of the isotherm models for Pb(II) adsorption on different MH particles

	Langmuir model			Freundlich model		
Sample	q_m (mg g^{-1})	k_L (L mg^{-1})	R^2	$1/n$	k_F (mg g^{-1})	R^2
FGMH	2612	0.0977	0.9989	0.1643	1075	0.9941
HPMH	1431	0.0195	0.9960	0.3452	394	0.9699

Table 3 Different adsorbents and their maximum Pb(II) adsorption capacities

Sample	pH	Time (min)	Removal capability (mg g^{-1})	References
$Fe(OH)_3$ MS	—	80	75.64	25
MCs@Mg/Fe-LDHs	6.3	1440	755.27	26
$Mg(OH)_2$/GO	5.0	1440	344.4	27
CaAl-LDH	5.0	600	221.2	28
Hydroxyapatite	—	1440	26.52	29
Phosphate	—	1440	124.32	30
Flower like MgO	7	720	1980	31
Flower-like $Mg(OH)_2$	4.62	6	485.44	32
MH-CA20 (functionalized citric acid)	6	720	4545	23
FGMH	5	240	2612	This work
HPMH	5	240	1431	This work

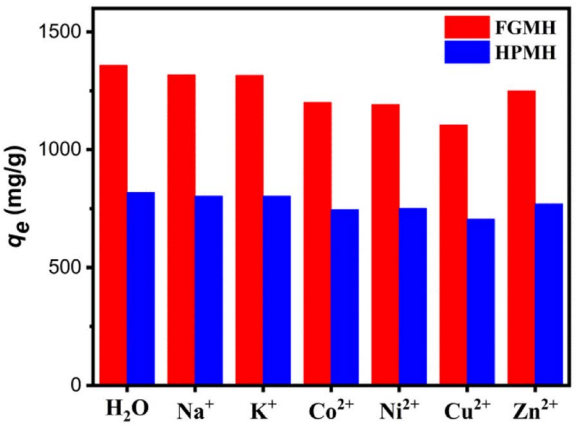

Fig. 8 Effect of coexisting cations on Pb(II) remove with FGMH and HPMH.

Fig. 9 illustrates the electrolytic recovery curve of Pb(II) ions over time. At the 120 min mark, the recovery efficiency of Pb(II) ions reached 96.5%. Fig. S1† displays the XRD pattern of the metal obtained through electrolysis. All diffraction peaks align with cubic-phase Pb (JCPDS#04-0686)[34] without any impurity peaks, signifying the high purity of the Pb metal obtained through electrolysis.

3.4 Mechanism discussion

To gain deeper insights into the removal mechanism of Pb(II) by MH, the variations in morphology and chemical composition of two types of MH were analyzed. Fig. 10 and 11 present SEM images and corresponding mapping analyses of FGMH and HPMH adsorbing Pb(II), respectively. It is evident that the flower ball structure of FGMH experiences slight damage after Pb(II) adsorption but maintains its 3D self-supporting structure. Conversely, HPMH retains its regular hexagonal sheet structure post-Pb(II) adsorption. The distribution of Pb elements in both adsorption products is uniform, with relatively strong signals, indicating that both morphologies of MH provide ample active sites for Pb(II) binding. Notably, after Pb(II) adsorption, the Mg element signal weakens, suggesting substantial exchange of Mg(II). However, the Mg element signal is still detectable in the product after Pb(II) adsorption by HPMH due to its thicker nanosheet layers and incomplete Mg(II) exchange. Additionally, strong C signals are detected in both solid products, suggesting the formation of carbon compounds during the adsorption process.

Fig. 12 illustrates the XRD patterns of the solid products after treating the Pb(II) solution with MH of two morphologies. The diffraction peaks of $Pb_3(CO_3)_2(OH)_2$ (JCPDS 13-00131)[35] were detected in both solid products, indicating that the adsorption products primarily consisted of Pb, C, and O elements. The presence of C elements during adsorption can be attributed solely to CO_2 dissolved in water, implicating CO_2 in the removal reaction. Additionally, after treating the Pb(II) solution with FGMH, the diffraction peak of the substance containing Mg(II) was barely detectable, indicating extensive Mg(II) exchange. However, the diffraction peak of MH was detected even after the Pb(II) solution was treated with HPMH, suggesting a cation exchange reaction from the surface of the nanosheet to the interior layer by layer.[36] Given that HPMH comprises relatively thick nanosheets, the deposited product ($Pb_3(CO_3)_2(OH)_2$) obstructs the exchange of Mg(II) in the inner layer. To confirm this, the

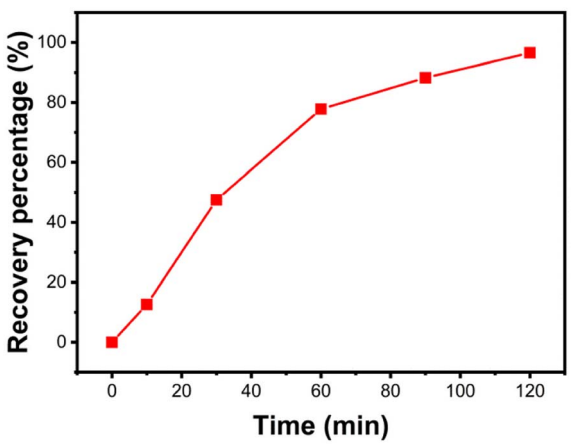

Fig. 9 Electrolytic recovery curve of Pb(II) ions over time.

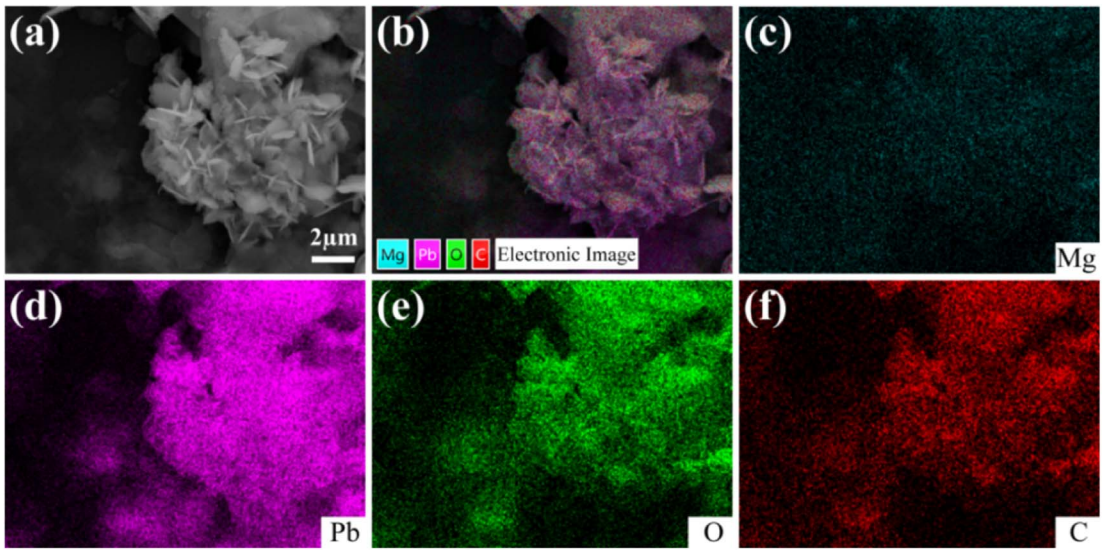

Fig. 10 SEM image of FGMH after adsorbing Pb(II) (a), along with the corresponding image (b) and elemental mapping analysis of (c) Mg, (d) Pb, (e) O, and (f) C.

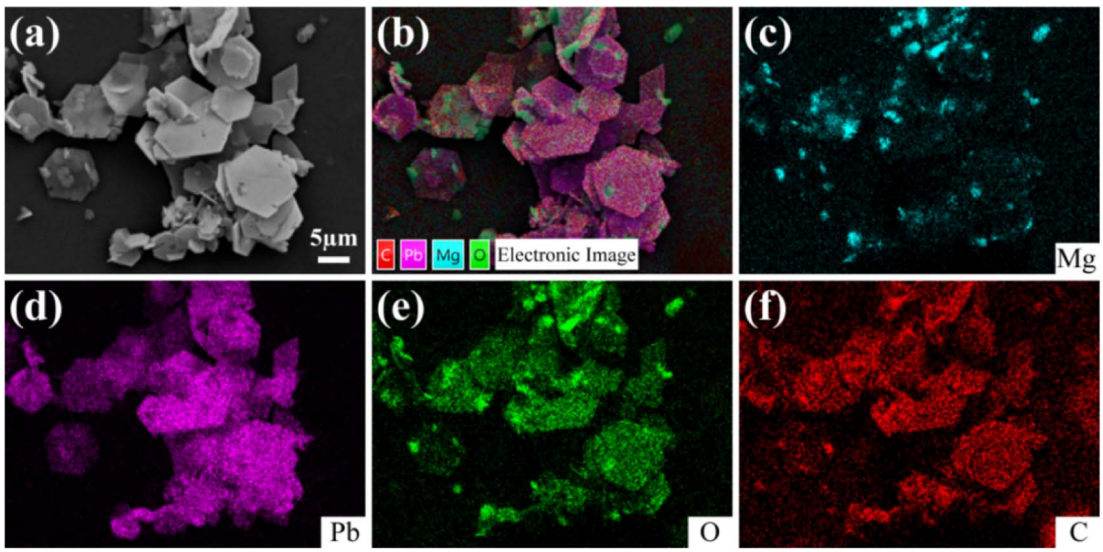

Fig. 11 SEM image of HPMH after adsorbing Pb(II) (a), along with the corresponding image (b) and elemental mapping analysis of (c) Mg, (d) Pb, (e) O, and (f) C.

concentrations of Mg(II) and Pb(II) ions in the solution at different time intervals were measured. The results revealed a linear relationship between the increase in Mg(II) ion concentration and the decrease in Pb(II) ion concentration in the solution (Fig. 13).

Based on the above analysis, the removal of Pb(II) by MH can be attributed to the following solid–liquid interface reaction:

$$Mg(OH)_2 + Pb^{2+} = Pb(OH)_2 + Mg^{2+} \quad (1)$$

$$3Pb(OH)_2 + CO_2 = Pb_3(CO_3)_2(OH)_2 + 2H_2O \quad (2)$$

Abundant Mg(II) and OH^- ions reside on the MH surface. When Pb(II) approaches the MH surface, it binds with OH^- to form $Pb(OH)_2$ on the MH surface *in situ*. Mg(II) is released into the solution, and Pb(II) takes its place within the MH lattice. The resulting $Pb(OH)_2$ is unstable and reacts with CO_2 dissolved in water to produce $Pb_3(CO_3)_2(OH)_2$. The deposited $Pb_3(CO_3)_2(OH)_2$ in the outer layer hinders the ionization of MH in the inner layer, and ion exchange ceases upon reaching a certain extent. Therefore, owing to its ultra-thin nanoflake composition, FGMH exhibits superior adsorption speed and capacity for Pb(II) compared to HPMH.

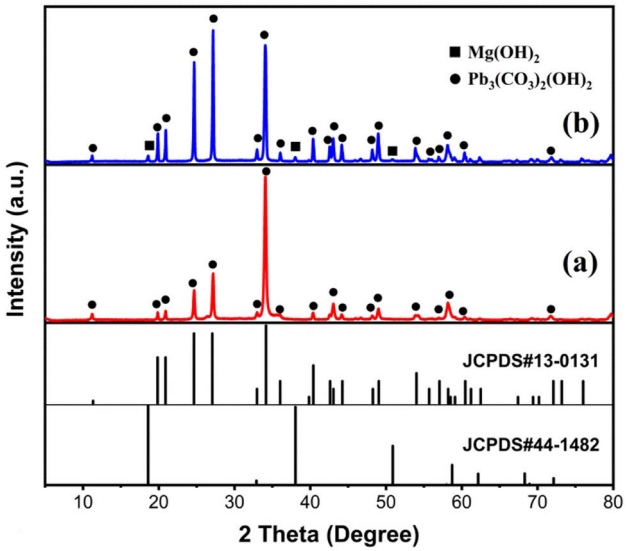

Fig. 12 XRD pattern of (a) FGMH and (b) HPMH after adsorbing Pb(II).

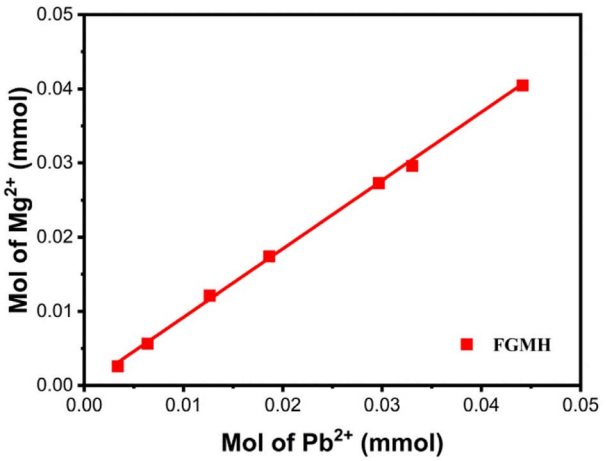

Fig. 13 Quantitative measurements of the amount of Mg(II) released and the amount of Pb(II) removed.

4. Conclusions

In this study, flower globular magnesium hydroxide (FGMH) and hexagonal plate magnesium hydroxide (HPMH) were successfully synthesized using different magnesium salts through the direct precipitation and hydrothermal methods, respectively. The adsorption capabilities of FGMH and HPMH for Pb(II) ions were compared. The adsorption processes of Pb(II) by both FGMH and HPMH adhered to the pseudo-second-order and Langmuir isotherm models. Notably, FGMH displayed superior Pb(II) ion adsorption performance, with a maximum adsorption capacity of 2612 mg g^{-1}, compared with HPMH (1431 mg g^{-1}). This difference can be attributed to the unique micro-morphology of FGMH, characterized by a flower ball structure composed of numerous MH nanosheets. This distinctive morphology provides an abundance of active sites and a larger specific surface area for enhanced adsorption. Furthermore, the feasibility of recycling adsorbed Pb(II) ions from MH through acid dissolution-electrolysis was demonstrated, achieving a remarkable recovery efficiency of 96.5%. The mechanism underlying the removal of Pb(II) ions can be attributed to the interaction between Pb(II) and OH^- ions on the MH surface, resulting in the formation of $Pb(OH)_2$ *in situ*. Subsequently, this compound can react with dissolved CO_2 to generate stable $Pb_3(CO_3)_2(OH)_2$, which adsorbs onto the MH surface.

Author contributions

Donghai Zhu: conceptualization, supervision and writing – review & editing, Jiachen Zhu: investigation, writing – original draft. Ping Li: investigation, data curation. Shengjie Lan: methodology, funding acquisition, and writing – review & editing.

Conflicts of interest

The authors declare no conflict of interest.

Acknowledgements

This study was financially supported by the Natural Science Foundation of Qinghai Province (Grant No. 2020-ZJ-934Q).

References

1 W. Yang, W. Cai, J. Zhou, C. Dang, X. Peng, Y. Chen, X. Wei, S. Bo, S. Liang and Z. Luo, *J. Environ. Chem. Eng.*, 2021, **9**, 106634.
2 W. M. Yin, Y. Wang, Y. C. Hou, Y. Sun, J. G. Zhang, H. L. Sun, S. J. Li, Q. J. Pan and Y. R. Guo, *Chem. Eng. J.*, 2020, **401**, 125961.
3 S. Arooj, S. Naz, A. Qaisar, S. Satti, A. Razzaq, A. F. Alrefaei, M. F. Albeshr, M. Durrani, S. F. Dai and R. U. Khan, *J. Appl. Anim. Res.*, 2023, **51**, 530–539.
4 Y. Fei and Y. H. Hu, *Chemosphere*, 2023, **335**, 139077.
5 P. K. Samantaray, S. Indrakumar, K. Chatterjee, V. Agarwal and S. Bose, *Nanoscale Adv.*, 2020, **2**, 2824–2834.
6 P. K. Samantaray, G. Madras and S. Bose, Next Generation Biomanufacturing Technologies, *Am. Chem. Soc.*, 2019, **1329**(14), 321–351.
7 X. X. Cheng, Y. R. Zhang, S. L. Shao, C. X. Lai, D. J. Wu, J. T. Xu, X. S. Luo, D. L. Xu, H. Liang and X. W. Zhu, *Desalination*, 2023, **548**, 116266.
8 L. Ulloa, M. Martinez-Minchero, E. Bringas, A. Cobo and M. F. San-Roman, *Sep. Purif. Technol.*, 2020, **253**, 117516.
9 T. K. Tran, K. F. Chiu, C. Y. Lin and H. J. Leu, *Int. J. Hydrogen Energy*, 2017, **42**, 27741–27748.
10 M. H. El Awady, M. A. Ahmed and A. Dahaba, *Egypt. J. Chem.*, 2020, **63**, 1697–1712.
11 S. Melhi, *Environ. Pollut. Bioavailability*, 2023, **35**, 2163922.
12 S. Gokila, T. Gomathi, P. N. Sudha and S. Anil, *Int. J. Biol. Macromol.*, 2017, **104**, 1459–1468.

13 P. M. Nekhunguni, N. T. Tavengwa and H. Tutu, *J. Environ. Manage.*, 2017, **204**, 571–582.
14 S. Q. Gu, X. N. Kang, L. Wang, E. Lichtfouse and C. Y. Wang, *Environ. Chem. Lett.*, 2019, **17**, 629–654.
15 Y. J. O. Asencios and M. R. Sun-Kou, *Appl. Surf. Sci.*, 2012, **258**, 10002–10011.
16 X. A. Bai, L. Y. Xing, N. Liu, N. A. Ma, K. X. Huang, D. P. Wu, M. M. Yin and K. Jiang, *Nanomaterials*, 2021, **11**, 3255.
17 M. Sivakumar, J. Widakdo, W. S. Hung, C. F. Wang, C. C. Hu, K. R. Lee and J. Y. Lai, *Sep. Purif. Technol.*, 2022, **288**, 120485.
18 J. F. Jin, J. S. Sun, K. H. Lv, X. B. Huang, J. T. Wang, J. P. Liu, Y. R. Bai, X. Guo, J. W. Zhao, J. Liu and Q. L. Hou, *J. Mol. Liq.*, 2021, **334**, 116087.
19 U. Upadhyay, I. Sreedhar, S. A. Singh, C. M. Patel and K. L. Anitha, *Carbohydr. Polym.*, 2021, **251**, 117000.
20 Y. S. Wang, Y. T. Chen, C. Liu, F. Yu, Y. L. Chi and C. L. Hu, *Chem. Eng. J.*, 2017, **316**, 936–950.
21 S. B. Jang, C. E. Choong, S. Pichiah, J. Y. Choi, Y. Yoon, E. H. Choi and M. Jang, *J. Hazard. Mater.*, 2022, **424**, 127267.
22 D. M. Jiang, Y. H. Yang, C. T. Huang, M. Y. Huang, J. J. Chen, T. D. Rao and X. Y. Ran, *J. Hazard. Mater.*, 2019, **373**, 131–140.
23 H. Zhu, L. Li, W. D. Chen, Y. J. Tong and X. S. Wang, *J. Hazard. Mater.*, 2021, **416**, 125922.
24 H. Amrulloh, Y. S. Kurniawan, C. Ichsan, J. Jelita, W. Simanjuntak, R. T. M. Situmeang and P. A. Krisbiantoro, *Colloids Surf., A*, 2021, **631**, 127687.
25 X. L. Zhao, Y. C. Su, S. B. Li, Y. J. Bi and X. J. Han, *J. Environ. Sci.*, 2018, **73**, 47–57.
26 Y. Y. Xie, X. Z. Yuan, Z. B. Wu, G. M. Zeng, L. B. Jiang, X. Peng and H. Li, *J. Colloid Interface Sci.*, 2019, **536**, 440–455.
27 P. P. Wang, Y. X. Ye, D. W. Liang, H. M. Sun, J. Liu, Z. F. Tian and C. H. Liang, *RSC Adv.*, 2016, **6**, 26977–26983.
28 W. Yao, J. Wang, P. Y. Wang, X. X. Wang, S. J. Yu, Y. D. Zou, J. Hou, T. Hayat, A. Alsaedi and X. K. Wang, *Environ. Pollut.*, 2017, **229**, 827–836.
29 A. I. Ivanets, N. V. Kitikova, I. L. Shashkova, M. Y. Roshchina, V. Srivastava and M. Sillanpää, *J. Water Process Eng.*, 2019, **32**, 100963.
30 A. Ivanets, N. Kitikova, I. Shashkova, Y. Matrunchik, L. Kul'bitskaya and M. Sillanpaa, *Environ. Technol. Innovation*, 2016, **6**, 152–164.
31 C. Y. Cao, J. Qu, F. Wei, H. Liu and W. G. Song, *ACS Appl. Mater. Interfaces*, 2012, **4**, 4283–4287.
32 X. Y. Shen, Y. X. Huang, H. M. Shao, Y. Wang, Q. Han, J. S. Chen, B. C. Li, Y. C. Zhai and T. Nonferr, *Metal. Soc.*, 2022, **32**, 3149–3162.
33 C. J. Li, Z. X. Li, J. K. Wang, W. B. Xiong, H. Yan, Y. L. Bai, D. Hare and Y. F. Zhao, *Chem. Eng. J.*, 2023, **462**, 141926.
34 Y. Izumi, F. Kiyotaki and Y. Seida, *J. Phys. Chem. B*, 2002, **106**, 1518–1520.
35 C. M. Xiong, W. Wang, F. T. Tan, F. Luo, J. G. Chen and X. L. Qiao, *J. Hazard. Mater.*, 2015, **299**, 664–674.
36 C. R. Li, Z. Y. Zhuang, F. Huang, Z. C. Wu, Y. P. Hong and Z. Lin, *ACS Appl. Mater. Interfaces*, 2013, **5**, 9719–9725.